Enhanced α-particle production from fusion evaporation reactions leading to ^{46}Ti

M. Cicerchia[1,2], F. Gramegna[1], D. Fabris[3], M. Cinausero[1], T. Marchi[1], G. Andreetta[2], S. Barlini[4,5], M. Bini[4,5], R. Bolzonella[2], M. Bruno[6]‡, A. Buccola[4,5], A. Caciolli[2,3], A. Camaiani[4,5], G. Casini[5], N. Cieplicka-Orynczak[7], G. Collazuol[2,3], M. D'Agostino[6], M. Degerlier[8], D. Dell'Aquila[9], L. Domenichetti[2], B. Fornal[7], C. Frosin[4,5], N. Gelli[5], D. Gruyer[10], V. L. Kravchuk[11], S. Leoni[12], I. Lombardo[13], J. Mabiala[14], M.V. Managlia[6], G. Mantovani[2,3,15], D. Mengoni[2,3], L. Morelli[6], A. Olmi[5], P. Ottanelli[4,5], G. Pasquali[4,5], G. Pastore[4,5], S. Piantelli[5], L. Scomparin[2], S. Valdré[5], G. Verde[14]

[1] INFN, Laboratori Nazionali di Legnaro, Legnaro (Pd), Italy. [2] Physics and Astronomy Department, Padova University, Padova, Italy. [3] INFN, Sezione di Padova, Padova, Italy. [4] Physics and Astronomy Department, University of Firenze, Firenze, Italy. [5] INFN, Sezione di Firenze, Firenze, Italy. [6] Physics and Astronomy Department, University of Bologna and INFN, Sezione di Bologna, Bologna, Italy. [7] Institute of Nuclear Physics, polish Academy of Science Krakow, Poland. [8] Science and Art Faculty Physics Department, Nevsehir Haci Bektas Veli University, Nevsehir, Turkey. [9] Dipartimento di Chimica e Farmacia, Università degli Studi di Sassari, Sassari, Italy and INFN, Laboratori Nazionali del Sud, Catania, Italy [10] Grand Accélérateur National d'Ions Lourds, 14076 Caen, France. [11] National Research Center "Kurchatov Institute", Moscow, Russia. [12] Physics and Astronomy Department, University of Milano and INFN, Sezione di Milano, Milano, Italy. [13] INFN, Sezione di Catania, Catania, Italy.[14] Department of Chemistry and Physics, Prairie View A&M University, Prairie View, TX 77446, USA. [15] Universidade de Santiago de Compostela, Santiago de Compostela, Spain.

E-mail: cicerchia@lnl.infn.it

September 2020

Abstract. In this paper, we report a detailed study on the de-excitation of the ^{46}Ti compound nucleus populated by means of four different reactions: ^{16}O+^{30}Si at 7 and 8 AMeV, ^{18}O+^{28}Si at 7 AMeV and ^{19}F+^{27}Al at 7 AMeV. The GARFIELD detection array was used to measure the light charged particles and the heavy fragments emitted. This setup covers a large fraction of the solid angle with high-granularity. Complete events are chosen through total charge (Z_{TOT}=22) detection. Fusion-evaporation events are selected based on the condition that only one heavy fragment is detected in coincidence with the light charged particles. The analysis of global observables, such as charge distribution and light charged particle multiplicities, is compatible with the

‡ deceased

formation of a thermalized compound nucleus for all the four reactions. Nevertheless, an enhanced emission of α-particles with respect to a pure statistical picture is observed at very forward angles (<20^o). This enhancement is mainly visible in the even-Z residue exit channels populated through the emission of only α-particles.

1. Introduction

The study of heavy-ion collisions at increasing bombarding energy allows to probe the properties of hot nuclei and the evolution of the reaction mechanisms [1]. In particular, the competition between short time-scale (i.e. fast, non-equilibrated) and long time-scale (i.e. thermally equilibrated) processes can be evidenced. Direct reactions, like break-up or nucleon transfer, and pre-equilibrium particle emission can be included among the short time-scale processes [2, 3, 4]. At bombarding energy above 10 AMeV, the pre-equilibrium particle emission becomes an increasingly important process [5, 6, 7, 8, 9, 10, 11, 12, 13]; such particles are forward focused and emitted in the very early stages of the collision before the full statistical equilibrium is achieved. The fast processes cannot be neglected also for energies lower than 10 AMeV because peculiar structures of the reaction partners may play an important role [14, 15]. Indeed, when nucleons as well as clusters of nucleons (like d, t, ^{3}He and α-particles) are emitted or captured in a nuclear collision, a strong correlation between nuclear structure and reaction dynamics is observed [16].

In recent years, our group has extensively studied the charged particle emission in nuclear collisions at bombarding energy from 10 to 20 AMeV, where the pre-equilibrium process is well established [17, 18, 19, 20, 21]. In these measurements, we focused on the effects that the structure of the colliding nuclei induces on the reaction dynamics and on the decay of the excited systems. Special attention was given to the α-cluster structure of the reaction partners. In this energy regime, however, disentangling the effects due to the pre-equilibrium itself from other mechanisms is not trivial. Within this framework, the present work aims to provide a benchmark in a lower energy region (< 10 AMeV), where the pre-equilibrium contribution to the particle emission is almost suppressed. Four reactions populating the same compound nucleus ^{46}Ti at different excitation energies were measured: ^{16}O+^{30}Si at 7 and 8 AMeV, ^{18}O+^{28}Si at 7 AMeV and ^{19}F+^{27}Al at 7 AMeV.

Preliminary results of this work were already reported in previously published conference proceedings. Issues of target contamination were encountered in the early phases of the analysis where the only condition applied for the data selection was the presence of at least one fragment with Z>11 [22, 23]. Later, the analysis of *Quasi-complete Events* ($Z_{tot} > 18$) allowed to remove completely the target contamination and to benchmark with high statistics the gross features of the reactions [24, 25]. Eventually, a preliminary analysis of the *Complete Events* ($Z_{tot} = 22$) was discussed [26, 27]. In the present paper, the selection of *Complete Events* is applied, and the final results are

Table 1. Main characteristics of the four studied reactions: beam and target; bombarding energy; entrance channel mass asymmetry: η = (A_T - A_P)/(A_T + A_P), where A_P and A_T are the projectile and target mass numbers, respectively; formed compound nucleus (CN) and its excitation energy (E^*_{CN}), in the hypothesis of complete fusion; center of mass velocity (v_{cm}); grazing angle (θ_{graz}); fusion cross-section, calculated using the Bass formula [28] (σ_{fus}); angular range (in the laboratory frame) of evaporation residues ($\Delta\theta^{lab}_{ER}$).

Reactions beam+target	E^{lab}_{beam} (AMeV)	η	CN	E^*_{CN} (MeV)	v_{cm} (cm/ns)	θ_{graz} (deg)	σ_{fus} (mb)	$\Delta\theta^{lab}_{ER}$ (deg)
$^{16}O+^{30}Si$	7	0.30	^{46}Ti	88.0	1.28	10.1	1081	0-30
$^{16}O+^{30}Si$	8	0.30	^{46}Ti	98.4	1.37	8.8	1070	0-30
$^{18}O+^{28}Si$	7	0.22	^{46}Ti	98.5	1.44	9.0	1110	0-28
$^{19}F+^{27}Al$	7	0.17	^{46}Ti	103.5	1.52	8.9	1100	0-28

presented for all the reactions under study. The thermal properties of the excited ^{46}Ti are reported. In addition, this work focuses on the detailed analysis of the exclusive output channels. The presented results are interpreted within the framework of the statistical model.

2. The experiment

The experiment was performed at the Legnaro National Laboratory (INFN, Italy). The beams were delivered by the TANDEM XTU electrostatic accelerator: ^{16}O at bombarding energies of 7 and 8 AMeV, ^{18}O at 7 AMeV and ^{19}F at 7 AMeV. These beams impinged onto three 100 μg/cm^2 thick self-supporting targets: ^{30}Si, ^{28}Si and ^{27}Al, respectively. The selected combinations of the four beams and targets led to the formation of the same excited compound nucleus, ^{46}Ti. Table 1 reports the main characteristics of the four reactions.

The same bombarding energy per nucleon (7 AMeV) has been chosen for the reactions $^{16}O+^{30}Si$, $^{18}O+^{28}Si$ and $^{19}F+^{27}Al$ in order to have the same pre-equilibrium component, which is known to be dependent on the beam velocity [16]. On the other hand, the choice of the bombarding energy of 8 AMeV for the reaction $^{16}O+^{30}Si$ was used to populate the compound nucleus at the same excitation energy of the reaction $^{18}O+^{28}Si$ at 7 AMeV. In this way, the same statistical component in the CN decay is expected for these two reactions.

2.1. Experimental setup

The experimental setup consists of the GARFIELD detector, covering almost completely the polar angles from 29.5^o to 150.4^o, and the Ring Counter (RCo) annular detector, centered at 0^o with respect to the beam direction and covering the forward angles in the range $5.5^o \leq \theta \leq 17.4^o$. The detailed description of the apparatus can be found in Ref [29]. Here only the main characteristics will be recalled.

The GARFIELD detector consists of two microstrip gas drift chambers, placed back to back, followed by CsI(Tl) scintillation detectors placed in the same gas volume. Light charged particles (LCP) and light fragments (LF) are detected and efficiently identified using different techniques. LCP (Z = 1, 2) are identified by Pulse Shape Analysis (PSA) in the CsI(Tl) scintillators, through the use of the *Fast* and *Slow* correlation. Good charge and mass separation were achieved in this experiment. The LF (Z = 3 to Z = 11) identification is performed using the $\Delta E - E$ technique from the microstrip and CsI(Tl) energy signals, with an energy resolution of 5%.

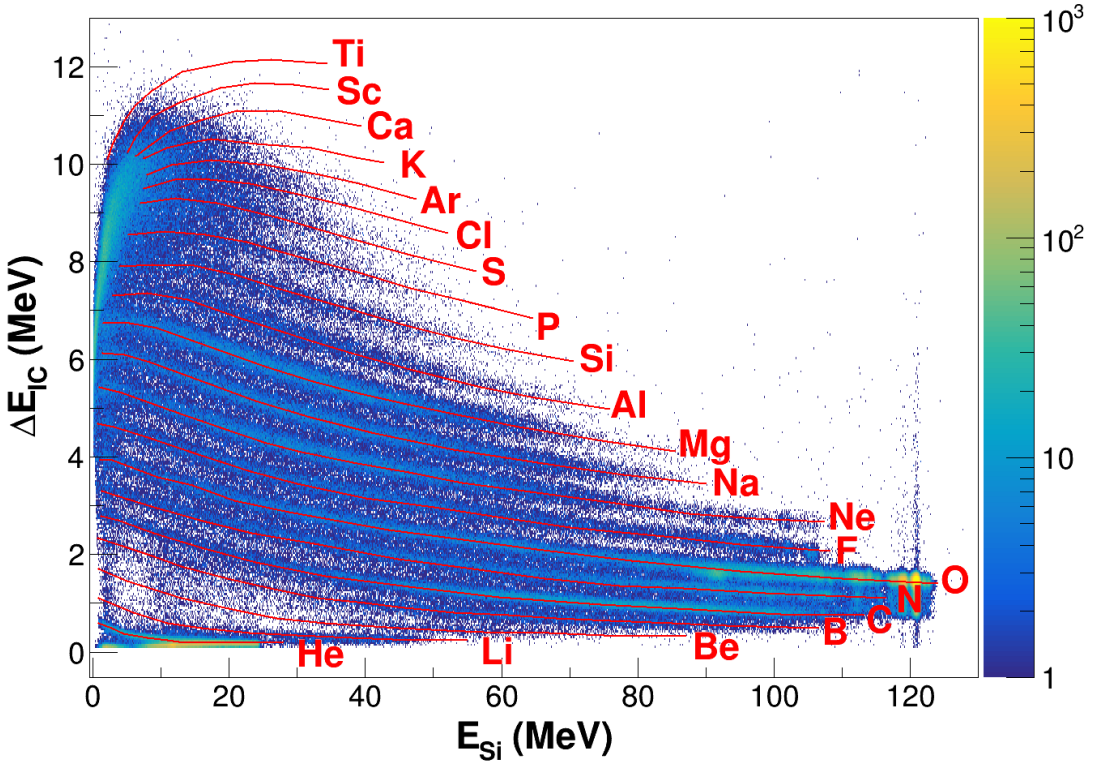

Figure 1. The $\Delta E - E$ correlations between ionization chamber and silicon pads in RCo for the reaction $^{16}O + ^{30}Si$ at 8 AMeV. The red lines over the ridges identify the nuclei: from He to Ti.

The RCo detector is an array of three-stage telescopes: the first is an ionization chamber (IC), the second a reverse mounted NTD silicon strip detector (8 strips) and the last a CsI(Tl) scintillator. In this experiment, the two inner strips were shielded with a thick aluminum foil in order to prevent radiation damage effects in detectors by the elastically scattered beam. The actually covered angular range is therefore $8.8^o \leq \theta \leq 17.4^o$. The reaction products with Z > 3 were stopped in the silicon layer and could be identified only in charge by the correlation $\Delta E - E$ between the energy loss in the gas stage (IC) and the residual energy in the silicon. Energy resolution of about 5% was achieved. An example of this correlation is shown in Fig. 1, where the region of heavier products corresponding mainly to Evaporation Residues (ER) can be observed at high

Table 2. List of used parameters for running G^{++} code. See text for details.

w	k_0	k_∞	a_κ	c_κ	J_η ($\hbar$)	η (MeV)
1.1	7.3	12	0.0517	0.0345	50	18.52

energy loss in the gas. For particles within the range $3 \leq Z \leq 7$, above an energy threshold of 3÷5 AMeV, a mass identification was also possible with Pulse Shape Analysis (PSA) in the silicon pads thanks to their excellent energy resolution ($\sim 0.1\%$). Light particles punching through the silicon pads are identified both in charge and in mass with the $\Delta E - E$ correlation between silicon and CsI(Tl).

2.2. The simulation code: GEMINI^{++}

A set of simulations has been performed with the Monte Carlo statistical code GEMINI^{++} (G^{++}) [30]. This code is based on the Hauser-Feshbach formalism and describes the decay of the excited compound nucleus, explicitly considering the influence of spin and angular momentum on particle emission. Table 2 summarizes the values used for the key parameters in the G^{++} calculation. The parameter w takes into account the thermal fluctuations of the *emission barrier*. The barrier is estimated averaging over transmission coefficients calculated for three different nuclear radii: R_0 (spherical nucleus) and $R_0 \pm \delta r$. δr is evaluated as $w\sqrt{T}$, where T is the nuclear temperature of the daughter nucleus. The parameters k_0, k_∞, a_κ and c_κ allow to calculate the effective *level density* parameter as a function of the excitation energies: $a_{eff}(E^*) = \frac{A}{k_\infty - (k_\infty - k_0) exp\left\{-\frac{\kappa(A)}{k_\infty - k_0}\frac{E^*}{A}\right\}}$. k_0 and k_∞ give the asymptotic values at low and high excitation energy: $\frac{A}{k_0}$ and $\frac{A}{k_\infty}$. a_κ and c_κ are needed to calculate how fast the long range correlation washes out with excitation energy through the function $\kappa(A) = a_\kappa e^{c_\kappa A}$. Shell corrections to the level density are taken into account through the parameters η and J_η. The Sierk parametrization of the yrast line has been adopted in this work to take into account the well known deformation of the excited $^{46}Ti^*$ nucleus [31].

The simulated events were filtered through a software replica of the GARFIELD + RCo apparatus which reproduces all the detection conditions (geometry, energy thresholds, energy resolution, etc.). In this way a direct comparison with the experimental data can be performed. Figure 2 shows the correlation plots between energy and emission angles in the laboratory frame for the ER. The left panels display the 4π correlations, while the right ones show the effects of the software filter. As a result, the filtered ER angular distributions are limited to the angular coverage of the RCo ($8.8^o \div 17.4^o$). Moreover, the ER energy has a lower limit, due to the identification threshold, at $\sim$ 25 MeV (that is $\sim 0.6 \div 0.8$ AMeV). In fact, since we have selected charge-identified evaporation residues, they have to cross the ionization chamber and stop in the silicon detector in order to fill the ΔE-E correlation. Figure 2 demonstrates that, in spite of the energy and geometrical cuts caused by the experimental apparatus,

the peak of the ER distribution is within our detection capabilities.

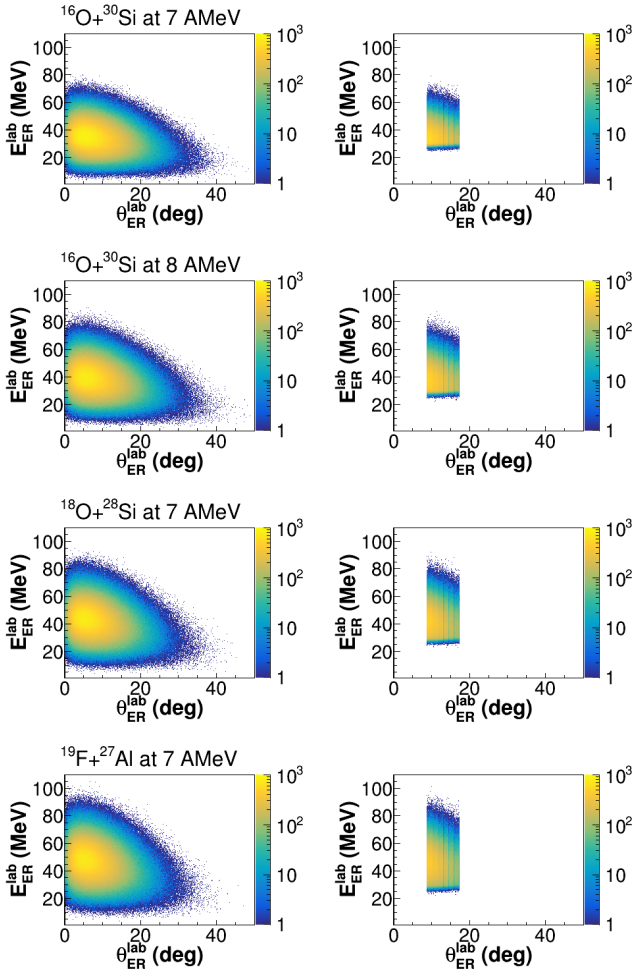

Figure 2. Two-dimensional plots of residues laboratory energy vs. their laboratory emission angle as predicted by G^{++} without (left panels) and with (right panels) geometrical filter. From top to bottom, the four studied reactions ^{16}O+^{30}Si at 7 AMeV, ^{16}O+^{30}Si at 8 AMeV, ^{18}O+^{28}Si at 7 AMeV and ^{19}F+^{27}Al at 7 AMeV.

2.3. Events Selection

We focused the present analysis on central collisions leading to complete fusion-evaporation reactions. To this purpose a strict selection of the detected events has been applied.

Figure 3 reports the experimental correlation plots between the charge (Z) and the energy (E_{lab}) of the detected particles (panel *(a)*) and between the total charge (Z_{TOT}) and the longitudinal momentum (q_z/q_{beam}) for each detected event (panel *(b)*). The correlations are shown for the reaction ^{16}O+^{30}Si at 8 AMeV, but similar results are obtained for the other three reactions.

Complete events and most dissipative collisions are selected with the conditions that, in each event, the total detected charge is $Z_{TOT} = 22$ (i.e. the total charge of

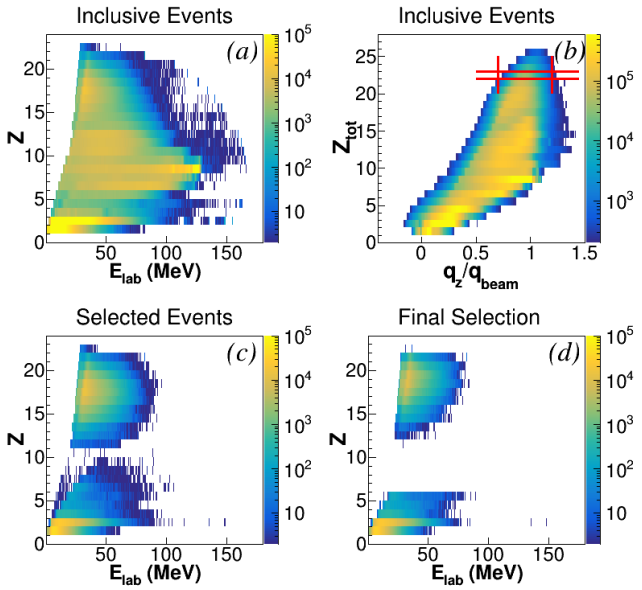

Figure 3. Experimental plots for the reaction ^{16}O+^{30}Si at 8 AMeV. Panels *(a)* and *(b)* show the Z vs. E_{lab} and the Z_{tot} vs. q_z/q_{beam} correlations for the raw data set. Panels *(c)* and *(d)* respectively display the Z vs. E_{lab} correlations for the *complete events* selected by the red gate in panel *(b)* and after the request of the coincidence of LCP with one heavy fragment.

the entrance channel) and that the average longitudinal momentum, q_z/q_{beam}, is within the limits 0.7-1.2 as shown in Fig. 3 *(b)*. Figure 3 *(c)* illustrates the effect of the gate selection on the charge vs energy correlation. Selecting the complete charge events (Z_{TOT} = 22), all quasi-elastic and almost all peripheral collisions have been removed since only partial charge could be detected for those events. Indeed, the heavy partner is normally stopped either within the target or inside any dead layer of the detector. This is shown in Fig. 3 *(c)*, where all fragments with charge around Z = 8 have been cut, as expected.

To further clean our set of data, the coincidence between LCP or LF (Z < 6) detected in the whole apparatus (GARFIELD + RCo), and only one heavy fragment with Z > 12, detected in the RCo, has been required. In this way, events from fusion-fission and/or deep inelastic collisions are suppressed. The correlation between charge and energy of our final data set is displayed in Fig. 3 *(d)*.

To check the data selection reliability, we have performed a complete G^{++} simulation of the four reactions. The same conditions described above have been applied to the total generated events, which have also been filtered with the software replica of the apparatus. This is illustrated in Fig. 4, for the reaction ^{16}O+^{30}Si at 8 AMeV, in analogy with the previous Fig. 3.

The comparison between panels *(a)* and *(b)* of Fig. 3 and of Fig. 4 shows a strong contribution, in the experimental data, of reaction channels in which fragments with charge close to Z = 8 (i.e. the oxygen beam) are emitted. As mentioned above, these

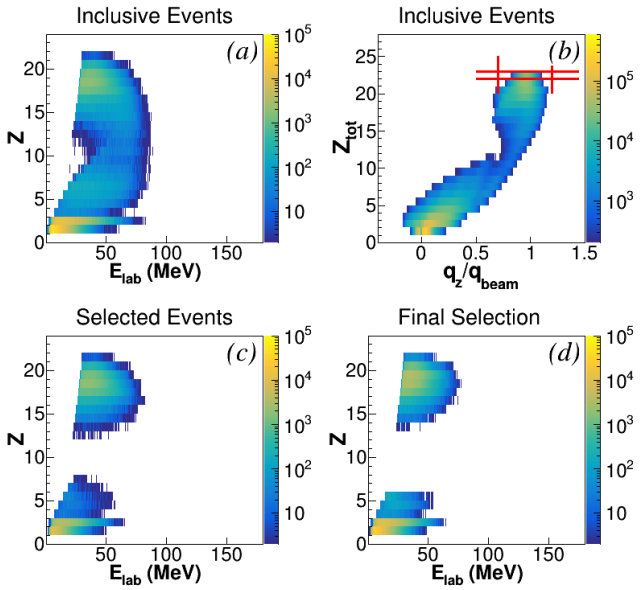

Figure 4. Same of Fig. 3 but for simulated events.

fragments are related to elastic and quasi-elastic scattering and peripheral collisions with exchange of few nucleons between the reaction partners. This contribution is obviously not present in the simulated data since only the decay of the CN is considered in the G^{++} code.

In addition, the experimental data present an extra yield of reacted particles due to oxygen contamination in the used targets. This relevant feature has been further investigated and verified through elemental analysis techniques. In particular, using the Rutherford Back Scattering method, fractions between 30% and 50% of ^{nat}O have been found. The decay products emitted by the reactions on the target contaminants have similar characteristics as the products from quasi-elastic scattering and peripheral collisions of the reactions under study. This is demonstrated by an additional G^{++} simulation. As an example, in Fig. 5 the Z vs. E_{lab} plot for the contaminating reaction

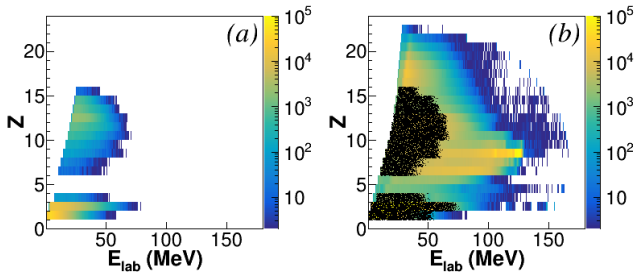

Figure 5. Correlation plot between Z and E_{lab} of the simulated events for the contaminant reaction ^{16}O+^{nat}O at 8 AMeV (panel *(a)*) and its comparison with the same experimental plot for the reaction ^{16}O+^{30}Si at 8 AMeV (panel *(b)*), already shown in Fig. 3.

^{16}O+^{nat}O at 8 AMeV is shown in panel *(a)*, while in panel *(b)* the simulated events are superimposed on the experimental plot of reaction ^{16}O+^{30}Si at 8 AMeV.

As one can notice in the panels *(c)* and *(d)* of Figs. 3 and 4, with the application of the very strict conditions on the data selection, the reactions on the contaminants are rejected together with unwanted peripheral events. The final result is a rather clean class of events. Hereafter, we will refer to these selected data as *Complete Events*.

3. Data analysis: *Complete Events*

Despite the fact that the *Complete Events* represent only 0.5% of the total statistics, we were able to perform a complete analysis of this data set as illustrated in the rest of the discussion. The total amount of selected events is about 0.2, 0.6, 0.5 and 0.7 millions for the reactions ^{16}O+^{30}Si at 7 AMeV, ^{16}O+^{30}Si at 8 AMeV, ^{18}O+^{28}Si at 7 AMeV and ^{19}F+^{27}Al at 7 AMeV, respectively.

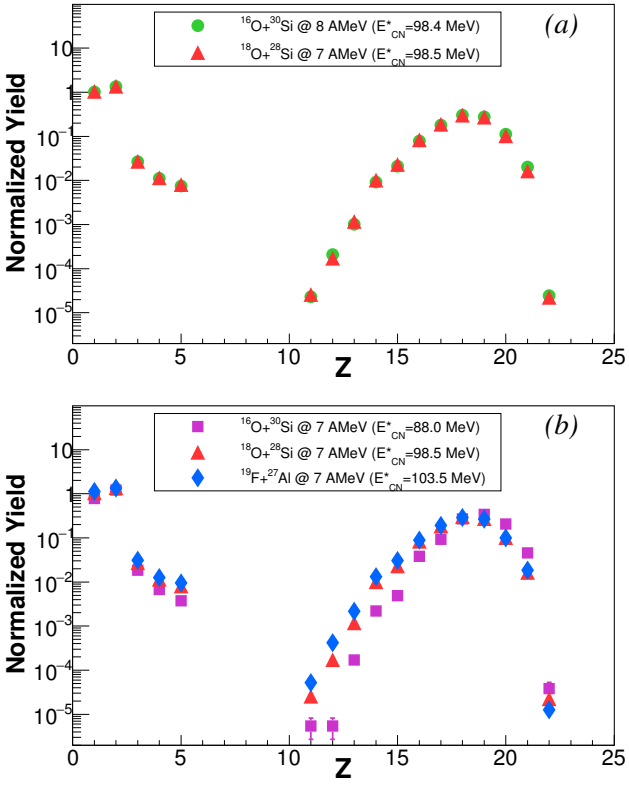

Figure 6. Experimental charge distributions: *(a)* comparison of the two reactions populating the CN at the same excitation energy: ^{16}O+^{30}Si at 8 AMeV (E^*_{CN} = 98.4 MeV) in green dots and ^{18}O+^{28}Si at 7 AMeV (E^*_{CN} = 98.5 MeV) in red triangles; *(b)* comparison of reactions with the same bombarding energy: ^{16}O+^{30}Si at 7 AMeV (E^*_{CN} = 88.0 MeV) in magenta squares, ^{18}O+^{28}Si at 7 AMeV (E^*_{CN} = 98.5 MeV) in red triangles and ^{19}F+^{27}Al at 7 AMeV (E^*_{CN} = 103.5 MeV) in blue diamonds. The distributions are normalized to the total number of the *Complete Events*.

The fragment charge distribution of the *Complete Events* has been studied as a

function of the CN excitation energy. In Fig. 6 *(a)* the distributions related to the reactions ^{16}O+^{30}Si at 8 AMeV and ^{18}O+^{28}Si at 7 AMeV populating the ^{46}Ti at the same excitation energy (E^*_{CN} = 98.5 MeV) are presented. The two distributions are identical, as expected for a fully statistical de-excitation of the CN. Fig. 6 *(b)*, the reactions ^{16}O+^{30}Si at 7 AMeV, ^{18}O+^{28}Si at 7 AMeV and ^{19}F+^{27}Al at 7 AMeV are compared. Again, as expected for a pure statistical decay, the increase in E^*_{CN} from 88 MeV (^{16}O+^{30}Si at 7 AMeV) to 103 MeV (^{19}F+^{27}Al at 7 AMeV) leads to longer decay chains. Consequently, the number of emitted LCP (1≤Z≤2) and LF (3≤Z≤5) increases, while the ER distribution is shifted toward lower Z. In fact, with increasing E^*_{CN} the yields of the heavy ER (Z≥18) increase, while for light ER the trend is reversed. In addition, Fig. 7 shows the comparison between the experimental ER charge distribution and the G^{++} simulation for the reaction ^{16}O+^{30}Si at 8 AMeV. The fair reproduction of the measured data, also observed for the other three reactions [32], further demonstrates the statistical behavior of the ^{46}Ti decay. This is also confirmed by the trend of the proton and α-particle multiplicities reported in Fig. 8. In fact, the higher particle multiplicity is favored when E^*_{CN} is increased.

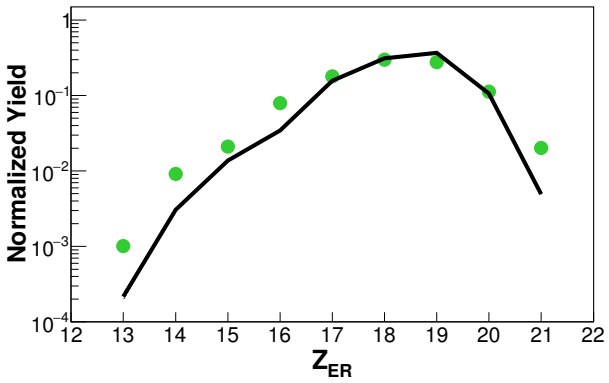

Figure 7. Comparison of experimental (points) and simulated G^{++} (line) charge distribution of evaporation residues for the reaction ^{16}O+^{30}Si at 8 AMeV. The experimental errors bars are inside the points.

Complementary information about the validity of the statistical decay picture can also be obtained from the analysis of the LCP energy spectra. In Fig. 9, the experimental energy spectra, for the four reactions, at backward ($97.5^o \leq \theta \leq 150^o$), middle ($29.5^o \leq \theta \leq 82.5^o$) and forward ($8.8^o \leq \theta \leq 17.4^o$) angles are compared with the G^{++} statistical code simulations. The spectra are normalized to the experimental maximum for a qualitative comparison of the shapes.

A fair reproduction of the proton spectra (upper panels of Fig. 9) is achieved in the whole angular range, with the exception of the high energy tail in the middle angular range. In the same region the shapes of the α-particle spectra are reproduced as far as the Coulomb barrier is concerned (panel *(e)*), while the tails are not well described.

On the other hand, the α spectra are reasonably reproduced at GARFIELD backward angles (panel *(d)*) for all the reactions and at RCo angles (panel *(f)*) except

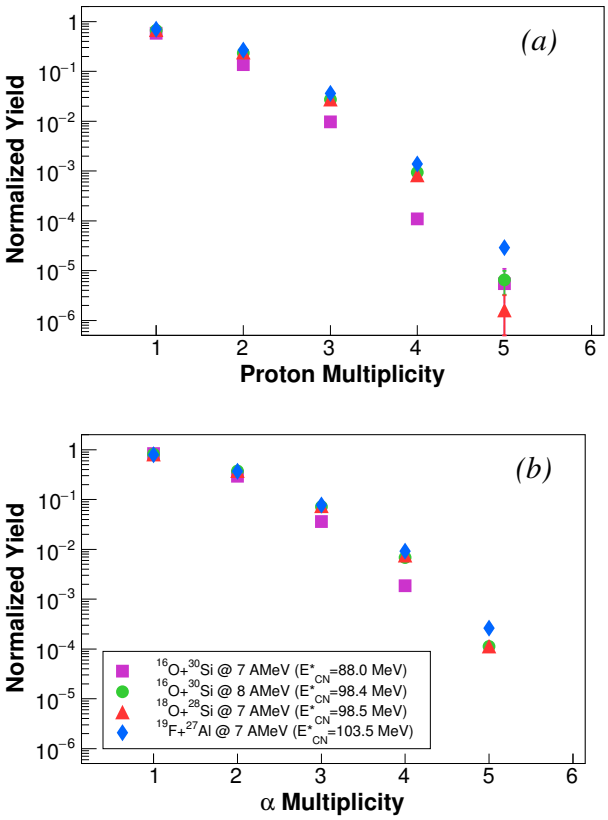

Figure 8. Experimental multiplicities: *(a)* for protons and *(b)* for α-particles. Comparison of the four reactions: ^{16}O+^{30}Si at 7 AMeV (E^*_{CN} = 88.0 MeV) in magenta squares, ^{16}O+^{30}Si at 8 AMeV (E^*_{CN} = 98.4 MeV) in green dots, ^{18}O+^{28}Si at 7 AMeV (E^*_{CN} = 98.5 MeV) in red triangles and ^{19}F+^{27}Al at 7 AMeV (E^*_{CN} = 103.5 MeV) in blue diamonds. The distributions are normalized to the total number of the *Complete Events*.

for the reaction ^{16}O+^{30}Si at 8 AMeV which is the one at the higher beam energy per nucleon (8 AMeV). In this case, the enhancement of the high energy tail could be related to the onset of pre-equilibrium emission [9]. This is also supported by the comparison with the reaction ^{18}O+^{28}Si at 7 AMeV that populates the ^{46}Ti at the same E^*_{CN}. Furthermore, the increase of the entrance channel mass asymmetry could also favor the pre-equilibrium emission in the reaction ^{16}O+^{30}Si at 8 AMeV with respect to ^{18}O+^{28}Si at 7 AMeV [16]. To sum it up, the G^{++} calculations performed using the set of parameters defined in Table 2 are able to reproduce the trend of all the spectra close to the Coulomb barrier, while some discrepancies are observed on the tails.

Deviations from a pure statistical behavior are observed comparing the LCP experimental angular distributions in the laboratory frame with the predictions of the statistical code G^{++}. Those comparisons are reported in Fig. 10 *(a)* for the α-particles emitted from all the reactions. The distributions are normalized to the solid angles and to the total number of ER (i.e., the number of events). The G^{++} statistical code reproduces well the data in the GARFIELD angular range ($29.5^o \leq \theta \leq 150^o$). In

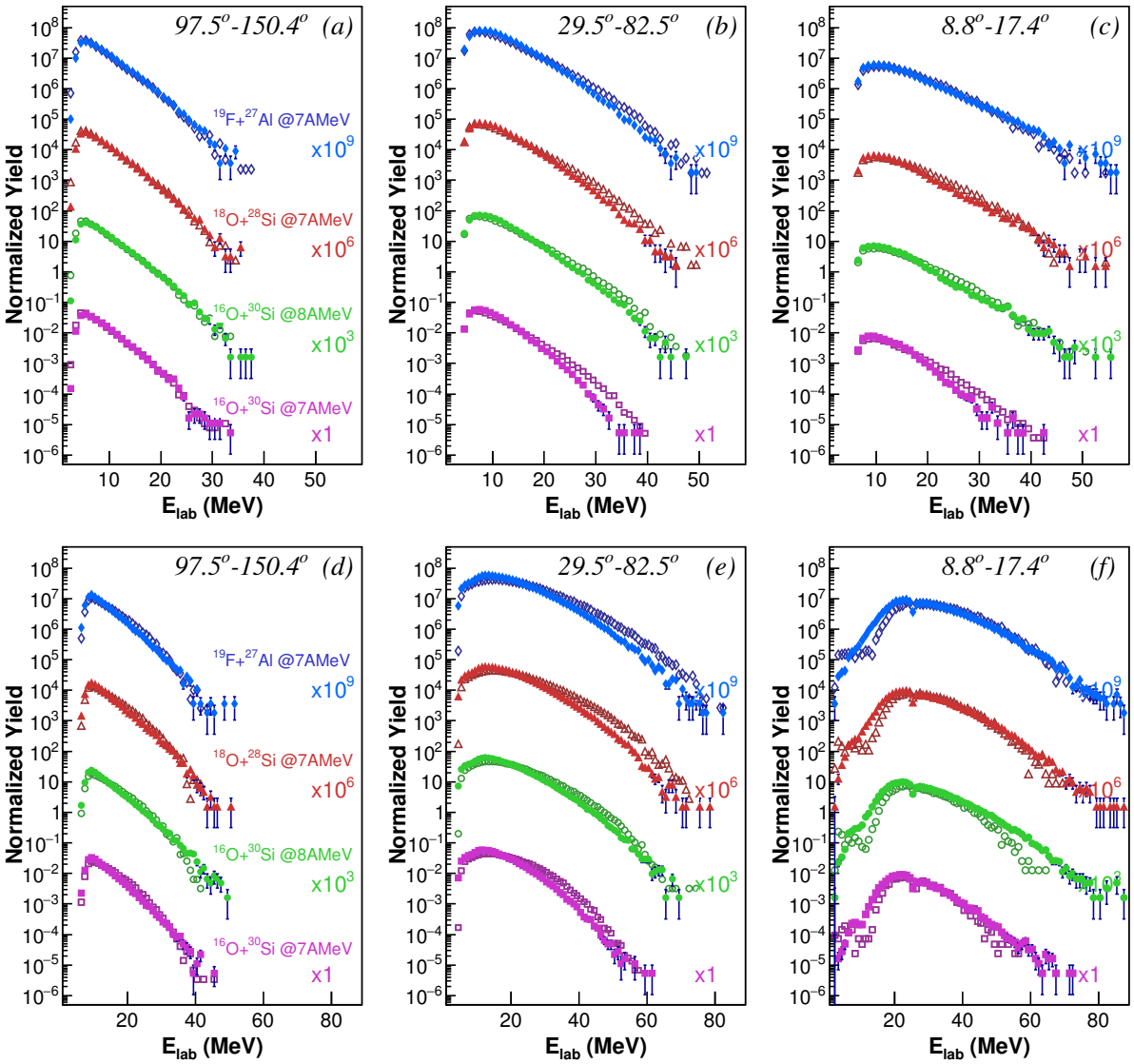

Figure 9. Experimental (full symbols) protons (upper panels) and α-particles (lower panels) energy spectra compared with G^{++} simulations (open symbols) in the three angular regions: $8.8^o \div 17.4^o$ in *(c)* and *(f)* panels, $29.5^o \div 82.5^o$ in the *(b)* and *(e)* panels and $97.5^o \div 150.4^o$ in *(a)* and *(d)*. The simulated spectra are normalized to the experimental maximum. The four reactions are shown with different colors: ^{16}O+^{30}Si at 7 AMeV ($E^*_{CN} = 88.0$ MeV) in magenta squares, ^{16}O+^{30}Si at 8 AMeV ($E^*_{CN} = 98.4$ MeV) in green dots, ^{18}O+^{28}Si at 7 AMeV ($E^*_{CN} = 98.5$ MeV) in red triangles and ^{19}F+^{27}Al at 7 AMeV ($E^*_{CN} = 103.5$ MeV) in blue diamonds and they are, respectively, plotted with a multiplication factor of 1, 10^3, 10^6 and 10^9.

particular, the kinematic boost due to the center of mass velocity is well accounted for by the simulations, being the emitted α-particles more forward-focused when v_{cm} increases. On the other hand, the G^{++} calculations fail in reproducing the data in the very forward angular range covered by the RCo ($8.8^o \leq \theta \leq 17.4^o$). In particular, G^{++} strongly underestimates the number of particles emitted at these angles. In Fig. 10 *(b)*, the $8.8^o \leq \theta \leq 17.4^o$ zone is expanded for a better view. As it can be seen,

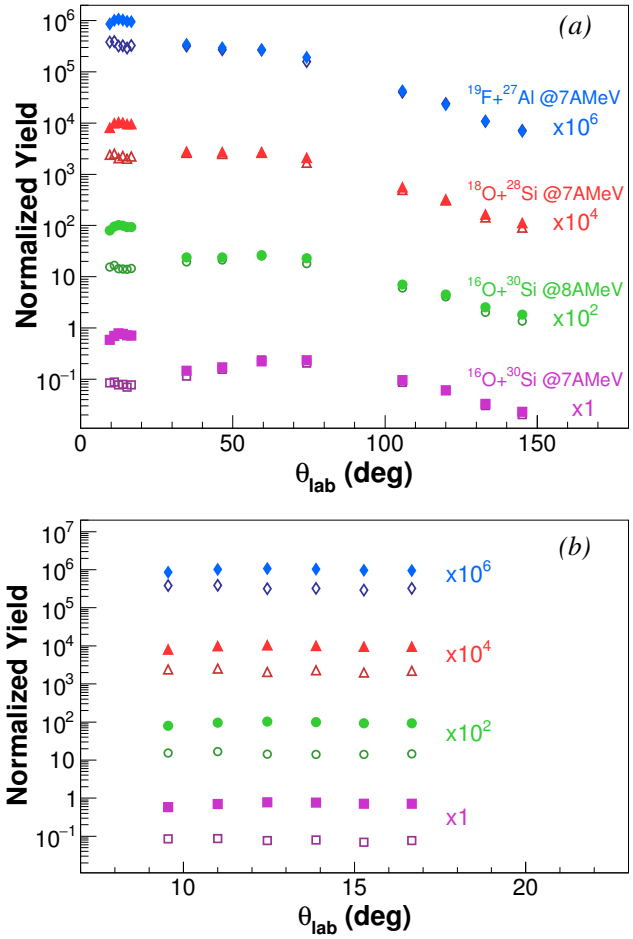

Figure 10. Comparison of α-particles angular distributions: experimental (full symbols) vs. G^{++} simulation (open symbols) for the four studied reactions. The reaction $^{16}O+^{30}Si$ at 7 AMeV (E^*_{CN} = 88.0 MeV, v_{cm} = 1.28 cm/ns) is drawn in magenta squares. The plots of the reactions $^{16}O+^{30}Si$ at 8 AMeV (E^*_{CN} = 98.4 MeV, v_{cm} = 1.37 cm/ns) in green dots, $^{18}O+^{28}Si$ at 7 AMeV (E^*_{CN} = 98.5 MeV, v_{cm} = 1.44 cm/ns) in red triangles and $^{19}F+^{27}Al$ at 7 AMeV (E^*_{CN} = 103.5 MeV, v_{cm} = 1.52 cm/ns) in blue diamonds are drawn with a multiplication factor of, respectively, 10^2, 10^4 and 10^6. In panel *(a)* the whole angular distribution is shown; while, in panel *(b)* the zoom on the very forward angles (RCo) is presented. The distributions are normalized to the number of *Complete Events* and to the solid angles. The experimental error bars are within the points.

the overproduction of experimental α-particles appears to be very high for the reaction $^{16}O+^{30}Si$ at 7 AMeV and decreases as the CN excitation energy increases. Similar conclusions can also be drawn for the other emitted LCP. However, the experimental overproduction at forward angles is lower for deuteron, triton and ^3He with respect to the α-particles case and almost disappears for protons [32].

To quantify the extra amount of particles emitted with respect to a pure statistical picture, the ratios between the experimental and the G^{++} predicted particle yields ($Y_R^{\theta_{lab}}$) are reported in Fig. 11 for protons and α-particles as a function of the detection angle.

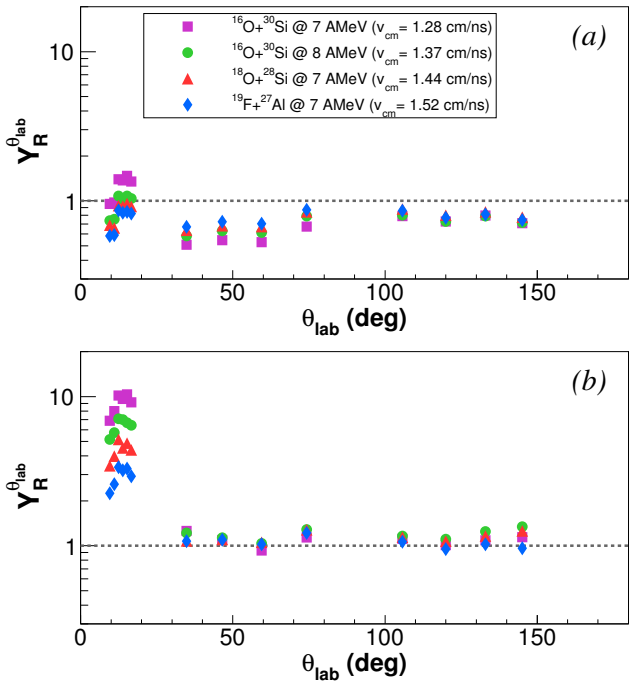

Figure 11. Comparison of the ratios between experimental and simulated yields as a function of the detection angle, for the four studied reactions: protons *(a)* and α-particles *(b)*. The four reactions are plotted with different colors: ^{16}O+^{30}Si at 7 AMeV (v_{cm} = 1.28 cm/ns) in magenta squares, ^{16}O+^{30}Si at 8 AMeV (v_{cm} = 1.37 cm/ns) in green dots, ^{18}O+^{28}Si at 7 AMeV (v_{cm} = 1.44 cm/ns) in red triangles and ^{19}F+^{27}Al at 7 AMeV (v_{cm} = 1.52 cm/ns) in blue diamonds. Before evaluating the ratio, the yields have been normalized to the number of events and to the solid angles. The errors bars are inside the points.

The proton yields are slightly overestimated by the model in the whole angular range (Fig. 11 *(a)*). This feature will be discussed with more details in Section 4. On the other hand, these ratios are almost 1 for the α-particle case (panel *(b)*) for $\theta \geq 29.5^o$, claiming for a statistical behaviour of the emission at larger angles. As already mentioned, for $8.8^o \leq \theta \leq 17.4^o$ we observe an overproduction of experimental α-particles corresponding to a factor of 2 to 10 higher than the statistical predictions. This factor increases as the CN excitation energy decreases. The observed trend is in clear contrast with the picture of an emission from a hot source during the thermalizzation.

4. Data analysis: Selected Exit Channels

To obtain more information on the behavior of the ^{46}Ti de-excitation, selected decay channels have been studied. Figures 12 *(a)* ÷ *(c)* show the ratios between experimental and simulated yields ($Y_R^{Z_{res}}$) of protons, emitted in coincidences with different residues (Z_{res}=13÷20) for the three angular regions: *(a)* 97.5^o ÷ 150.4^o, *(b)* 29.5^o ÷ 82.5^o and *(c)* 8.8^o ÷ 17.4^o. These ratios are reasonably accounted for by simulations with a general overestimation of the yields at all angles, in particular for Si (Z_{res}=14) and Ca (Z_{res}=20).

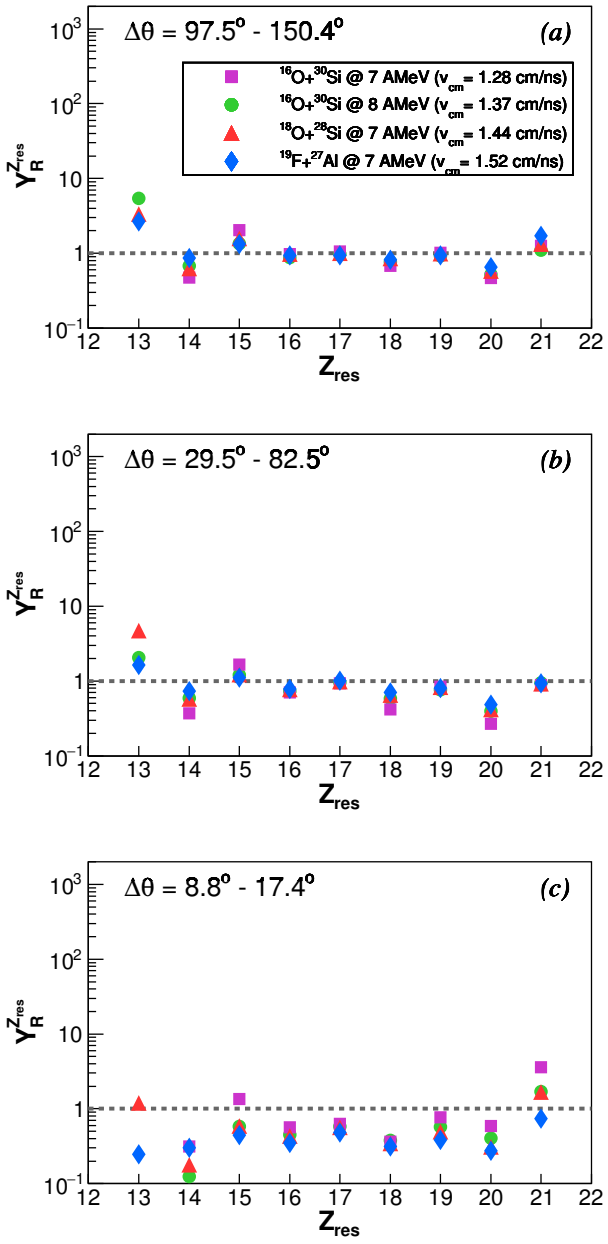

Figure 12. Comparison of the yields ratios ($Y_R^{Z_{res}}$) for protons emitted in coincidence with different residue vs. the charge of those residues in the three angular region: *(a)* $97.5^o \div 150.4^o$, *(b)* $29.5^o \div 82.5^o$ and *(c)* $8.8^o \div 17.4^o$. The usual color index is used for the four reactions: ^{16}O+^{30}Si at 7 AMeV magenta squares, ^{16}O+^{30}Si at 8 AMeV green dots, ^{18}O+^{28}Si at 7 AMeV red triangles, ^{19}F+^{27}Al at 7 AMeV blue diamonds. Before building the ratios, the yields have been normalized to the number of events.

An underestimation is evidenced for Al (Z_{res}=13) and Sc (Z_{res}=21). The behavior of the $Y_R^{Z_{res}}$ for α-particles is shown in Fig. 13 for the three angular regions. A fairly good reproduction of the experimental yield is obtained at $\theta \geq 29.5^o$, with the exception of α-particles in coincidence with Ca residues (Z_{res}=20), which are underestimated by the

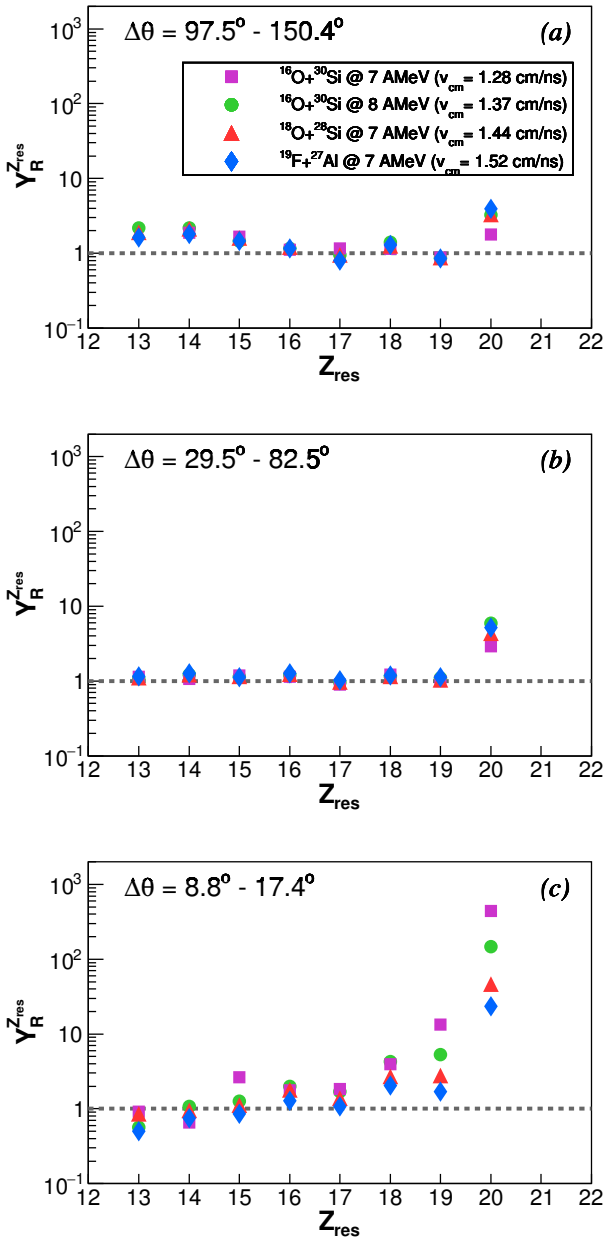

Figure 13. Same of Fig. 12, but for α-particles emitted in coincidences with different residues.

model. At very forward angles (Fig. 13 *(c)*) a strong underestimation of the model for the α-particles production is clearly visible for the heavier Z_{res}.

A complementary information can be obtained looking at the Branching Ratios (BR) of selected exit channels. The BR is defined as the ratio between the yield of a selected decay channel and the yield of the total channel populating the same final residue. In Table 3 the experimental BR (BR_{EXP}) for the main decay channels are compared with the G^{++} predictions ($BR_{G^{++}}$), for all reactions. Each channel is

Table 3. Experimental and simulated (G^{++}) branching ratio (BR) of the main channels for the four studied reactions. All channels are defined except for the number of emitted neutrons, which are not detected with our detection array.

channels	$^{16}O+^{30}Si$ at 7AMeV $BR_{EXP}(\%)$	at 7AMeV $BR_{G^{++}}(\%)$	$^{16}O+^{30}Si$ at 8AMeV $BR_{EXP}(\%)$	at 8AMeV $BR_{G^{++}}(\%)$	$^{18}O+^{28}Si$ at 7AMeV $BR_{EXP}(\%)$	at 7AMeV $BR_{G^{++}}(\%)$	$^{19}F+^{27}Al$ at 7AMeV $BR_{EXP}(\%)$	at 7AMeV $BR_{G^{++}}(\%)$
$^{45-x}_{21}$Sc+p+xn	92 ± 2	90	88 ± 2	88	88 ± 2	87	88 ± 2	84
$^{42-x}_{20}$Ca+α+xn	76.6 ± 0.9	29.6	60.8 ± 0.6	11.0	60.4 ± 0.6	13.4	53.4 ± 0.6	9.8
$^{44-x}_{20}$Ca+2p+xn	19.8 ± 0.3	60.9	30.6 ± 0.3	74.8	30.7 ± 0.4	70.8	35.6 ± 0.4	71.5
$^{41-x}_{19}$K+p+α+xn	91.8 ± 0.8	91.7	86.1 ± 0.5	78.8	85.9 ± 0.5	80.8	83.3 ± 0.5	74.5
$^{38-x}_{18}$Ar+2α+xn	63.7 ± 0.7	28.9	43.0 ± 0.3	11.68	39.6 ± 0.3	12.37	34.8 ± 0.3	8.56
$^{40-x}_{18}$Ar+2p+α+xn	30.6 ± 0.4	64.3	47.2 ± 0.3	78.1	50.0 ± 0.3	75.8	52.5 ± 0.3	77.4
$^{37-x}_{17}$Cl+p+2α+xn	86.4 ± 1.5	91.3	81.5 ± 0.6	84.8	81.4 ± 0.6	84.5	76.8 ± 0.6	79.6
$^{34-x}_{16}$S+3α+xn	83 ± 2	68	63.2 ± 0.7	42.7	60.3 ± 0.7	39.8	50.1 ± 0.6	28.3
$^{36-x}_{16}$S+2p+2α+xn	8.7 ± 0.5	9.1	26.0 ± 0.4	31.0	28.9 ± 0.4	31.2	37.5 ± 0.6	43.0
$^{33-x}_{15}$P+1p+3α+xn	49 ± 4	30	68.2 ± 1.4	52.5	71.0 ± 1.4	51.9	73.5 ± 1.3	60.1
$^{30-x}_{14}$Si+4α+xn	81 ± 9	67	70 ± 2	46	71 ± 2	49	62 ± 2	43
$^{32-x}_{14}$Si+3α+2p+xn	1.6 ± 0.8	1.6	5.2 ± 0.4	2.0	4.8 ± 0.4	2.4	9.5 ± 0.5	4.8
$^{29-x}_{13}$Al+4α+1p+xn	27 ± 15	-	32 ± 4	18	32 ± 3	13	40 ± 3	25

well defined except for the number of neutrons which are undetected in the present experiment. In the case of even Z residues (Ca, Ar, S and Si) also the BR for the competitive channel, where an α-particle is replaced by two protons, is reported.

In Fig. 14, the difference between experimental and simulated BR ($\Delta_{BR} = BR_{EXP}$ - $BR_{G^{++}}$) is depicted for the decay channels listed in Table 3. Δ_{BR} is quite large when the maximum number of α-particles is emitted in coincidence with even Z residues (up to $35\% \div 45\%$ for Ca and Ar). In the case of odd Z residue, however, the experimental BR is quite well reproduced by the simulations ($\Delta_{BR} \sim 0$). The present results show that decay channels in which the maximum number of α-particles is emitted seem to be experimentally favoured for even Z residues. This confirms the findings reported in Ref [33] for lighter nuclei.

For Ca and Ar residues the large positive Δ_{BR} for the channels corresponding to the maximum number of emitted α-particles is compensated by the negative Δ_{BR} corresponding to the channels in which one α-particle is replaced by the emission of two protons. This feature explains the overestimation of proton yields in the simulated angular distributions shown in Fig. 12 *(a)*.

The large positive Δ_{BR} for maximum α-particle emission found in the case of longer α chains (i.e. 3α and 4α) related to S and Si residues, is compensated in the simulation by the opening of decay channels involving the emission of complex light fragments such as B and Be. This is illustrated in Fig. 15 which compares BR_{EXP} and $BR_{G^{++}}$ for all channels leading to the population of S and Si. In fact, in the case of S (Fig. 15 *(a)*) the simulations predict a sensitive enhancement of the channels Be+α+xn and

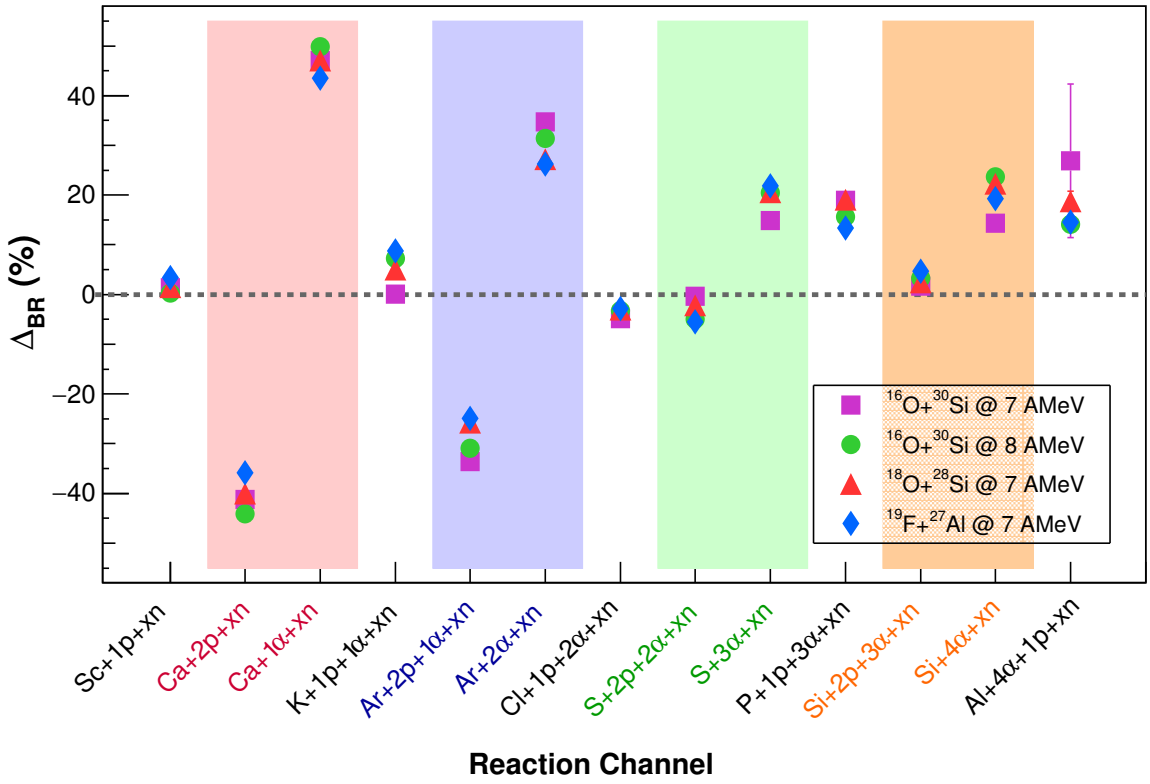

Figure 14. Comparison of the Δ_{BR} of the four studied reactions: ^{16}O+^{30}Si at 7 AMeV in magenta squares, ^{16}O+^{30}Si at 8 AMeV in green dots, ^{18}O+^{28}Si at 7 AMeV in red triangles and ^{19}F+^{27}Al at 7 AMeV in blue diamonds. The errors bars are inside the points. All the reported channels are selected except for the neutron emissions, which are not detected with our detection array.

B+p+xn. Similarly, for the Si residue the B+α+p+xn channel is strongly populated in the simulations.

5. Summary and conclusions

The excited ^{46}Ti compound nucleus has been populated through four different heavy-ion reactions at bombarding energies close to the threshold for the onset of pre-equilibrium. Light charged particle emission was studied in coincidence with evaporation residues for events in which the total charge of the entrance channel has been reconstructed.

The charge distributions and the light charged particle multiplicities show the expected trend for the decay from a thermalized source. In particular, the charge distributions for the two reactions which populate the ^{46}Ti at the same excitation energy are consistent. In addition, GEMINI^{++} statistical model calculation fairly reproduces the evaporation residue charge distribution and the particle energy spectra for all the studied reactions.

The angular distributions of the light charged particles at angles larger than 29.5^o,

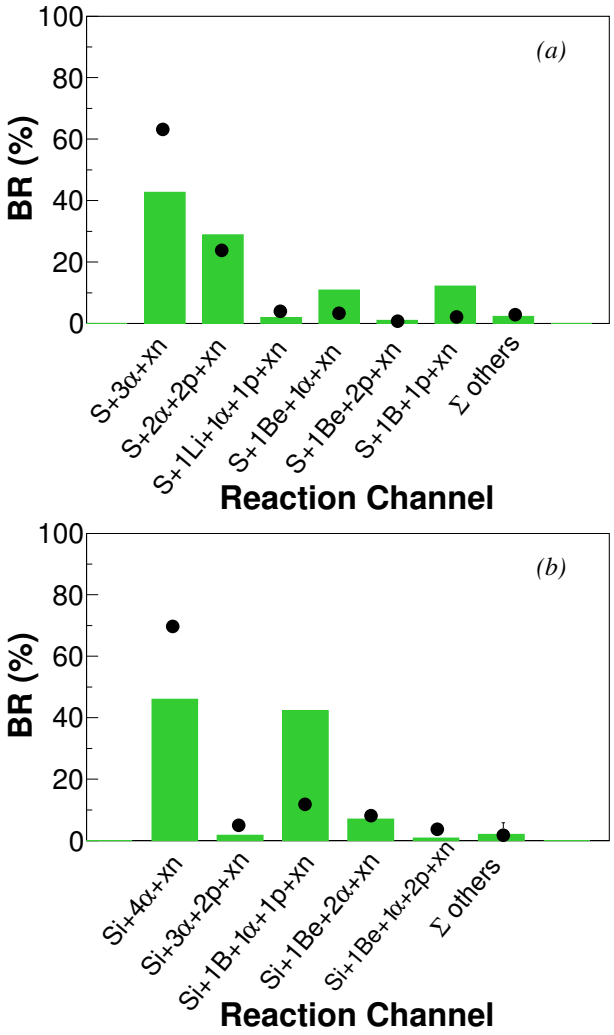

Figure 15. Comparison of the BR for the most important channels with *(a)* S and *(b)* Si residues for the reaction $^{16}O+^{30}Si$ at 8 AMeV. The green dots are the experimental BR while the histograms represent the simulated data. The experimental error bars are inside the points.

are in agreement with the predictions of the statistical model. An enhanced α-particle production at forward angles (lower than 20^o) has been, however, pointed out for all the reactions. This extra amount of particles decreases as the excitation energy of the compound nucleus increases, at odds with what expected for a pre-equilibrim emission.

This observed α-particle overproduction is mainly related to the population of the higher Z residues. In addition, the comparison of the measured branching ratios with GEMINI^{++} predictions shows peculiar behavior for the exit channels where only α-particles (and possibly neutrons) are emitted. The analysis shows that an excess in the yield of those channels is compensated by a defect in the competing ones. This is a common feature that underlines the importance of nuclear structure effects in the decay of the α-conjugated compound nucleus.

Bibliography

[1] A. J. Konig and J. M. Akkermans, *Pre-equilibrium nuclear reactions: An introduction to classical and quantum-mechanical models.* World Scientific, Singapore (1999).
[2] M. Nandy et al., Phys. Rev. C 60 (1999) 044607.
[3] P. L. Gonthier, Phys. Rev. C 35 (1987) 1946.
[4] W. D. M. Rae et al., Phys. Rev. C 30 (1984) 158.
[5] M. P. Kelly et al., Phys. Rev. C 56 (1997) 3201.
[6] D. Shapira et al., Phys. Rev. C 55 (1997) 2448.
[7] J. Gomez del Campo et al., Phys. Rev. C 60 (1999) 021601; Phys. Rev. C 53 (1996) 222.
[8] K. A. Griffioen et al., Phys. Rev. C 37 (1988) 2502.
[9] J. Cabrera, Phys. Rev. C 68 (2003) 034613-1.
[10] L. Lassen, Phys. Rev. C 55 (1997) 1900.
[11] S. Valdré et al., Phys. Rev. C 93 (2016) 034617.
[12] X. Campi et al., Phys. Lett. B 142 (1984) 8.
[13] M. Blann, Phys. Rev. C 31 (1985) 1245.
[14] M. Cavinato et al. Phys. Rev. C 52 (1995) 2577.
[15] Mohd Shuaib et al. J. Phys. G: Nucl. Part. Phys. 44 (2017) 105108
[16] P. E. Hodgson et al., Phys. Rep. 374 (2003) 1 and ref. therein.
[17] V. L. Kravchuk, EPJ Web of Conferences 2 (2010) 10006.
[18] D. Fabris et al., Acta Phys. Pol. 46 (2015) 447.
[19] O. V. Fotina et al., Int. Jour. of Mod. Phys. E 19 (2010) 1134.
[20] O. V. Fotina et al., Phys. of Atom. Nucl. 73 (2010) 1317.
[21] T. Marchi *et al.*, in *Nuclear Particle Correlations and Cluster Physics* Ed. Wolf-Udo Schroeder, World Scintific (2017) 507-536.
[22] M. Cicerchia et al., J. Phys.: Conf. Ser. 863 (2017) 012057.
[23] F. Gramegna et al., EPJ Web of Conferences 163 (2017) 00020
[24] M. Cicerchia et al., J. Phys.: Conf. Ser. 966 (2018) 012062.
[25] M. Cicerchia, Nuovo Cimento C 41 (2018) 98.
[26] M. Cicerchia et al., Nuovo Cimento C 41 (2018) 187.
[27] M. Cicerchia et al., EPJ Web of Conferences 223 (2019) 01010
[28] R. Bass, Nucl. Phys. A 231 (1974) 45; Phys. Rev. Lett. 39 (1977) 265.
[29] M. Bruno *et al.*, Eur. Phys. J. A 49 (2013) 128.
[30] R. J. Charity, Phys. Rev. C 82 (2010) 014610; D. Mancusi et al., Phys. Rev. C 82 (2010) 044610.
[31] K. Mazurek et al., Phys. Rev. C 91 (2015) 034301.
[32] M. Cicerchia, PhD Thesis, University of Padova (2018).
[33] L. Morelli et al., J. Phys. G: Nucl. Part. Phys. 41 (2014) 075108.